ARCHIVES OF CIVIL AND MECHANICAL ENGINEERING

Vol. X 2010 No. 2

An analysis of the load-carrying capacity of elements subjected to complex stress states with a focus on the microstructural failure

P.G. KOSSAKOWSKI
Kielce University of Technology, Al. Tysiąclecia Państwa Polskiego 7, 25-314 Kielce, Poland.

The paper analyses the load-bearing capacity of S235JR steel elements subjected to complex stress states, taking into account the effect of microstructural damage. Assessing the material required conducting a microstructural analysis and standardized tensile strength tests. A modified Gurson–Tvergaard–Needelman (GTN) model was used to numerically analyse S235JR steel elements under the action of complex stresses. The results of the numerical analysis were reported to be consistent with those obtained during the strength tests. The method for the numerical calculations was described along with the admissible results and the criteria of failure for S235JR steel basing on the modified GTN model and the development of microdamage. As S235JR steel is a common structural material in Poland, the investigation results will be of use to a number of engineers and other specialists responsible for determining the load-carrying capacity and structural safety of elements or whole systems.

Keywords: *Gurson–Tvergaard–Needelman model, voids, numerical calculations, S235JR steel*

1. Introduction

While determining the structural safety of an element, it is necessary to measure the actual stresses and compare them with the admissible values defining the strength of the material. The analysis is relatively easy to conduct if an element is under the action of uniaxial stress. If complex stress states are involved, i.e. when the failure stress is a three-stress function, the analysis becomes more complicated. As the failure of a material (plastic deformation or fracture) is dependent on more than one major stresses, the safety of a structure can be assessed using the so called Huber strength hypotheses. The tensile stress of an element in the complex stress state is determined basing on the reduced stress compared to the failure stress, which is defined for structural steels according to the Huber–Mises (HM) hypothesis. A number of studies show that the HM model is not always suitable to analyse the plastic state in and beyond the range of deformations corresponding to the necking of an element subjected to tension. Assuming the continuum of the material, one cannot apply this model to establish the influence of the microstructural defects on the material strength. Such phenomena can be analysed using other models defining the relationship between the particular failure stages and the strength of the material.

One of the first models of this type was the Kachanov model [1], in which the failure parameter is defined as the damaged area divided by the unaffected area. Kachanov's approach was extended by Lemaitre, who introduced the potential elastic energy function to analyse the potential failure of the material [2–3]. Lemaitre's model was used mainly to describe creep rupture and fatigue of the materials. As the failure parameter is difficult to define, especially measure, the model was not appropriate for modeling the fracture phenomena for elements subjected to static or dynamic loads. Kachanov's model did not take into account the conditions of damage formation due to loading. The models by Kachanov and Lemaitre are some of the few used in elastic-plastic damage mechanics which take into consideration material failure. As suggested by Murakami in Ref. [4], the other models used for describing material damage are those of Gurson [5], Suquet [6], Cordebois and Sidoroff [7], Tvergaard [8–9], Rousselière [10–11], Dragon and Chihab [12], Chow and Lu [13], Voyiadjis and Katt [14], Murzewski [15],] Mou and Han [16], Saanouni [17], and Taper et al. [18]. In the recent years, the Gurson model, which links the degree of failure with the material structure, has been modified extensively.

The Gurson model for a porous solid [5], which is a modified Huber–Mises criterion, defines the influence of an increase in the void volume fraction on the strength of the material. This model was further modified by Tvergaard [19], and then by Tvergaard and Needleman [20–21]. The two scientists developed a method for the calculation of failure loads resulting from ductile fracture by considering selected microstructural parameters and plastic properties of a material, which is referred to as the GTN model. All the above mentioned models will be discussed further in this paper.

Damage in the form of voids occurs on the existing inclusions or separations. The growth and coalescence of these voids result in the development of localized plastic deformations. Many researchers suggest that the process of void growth is dependent on the state of stress, particularly the stress triaxiality ratio.

The cracking of polycrystalline structures is a complex issue. The processes of crack initiation and propagation are closely related to the material microstructure. There are three basic types of fracture mechanisms, i.e. brittle, shear and ductile. In shear and ductile fracture patterns, the cracking is attributable to the nucleation and coalescence of voids (see Figures 1 and 2) [22].

The current studies conducted by using the GTN model aim at determining microstructural parameters for different types of materials [23–28], analyzing the plasticity due to void initiation and growth, and defining the effect of voids on the load-carrying capacity of elements [29–39]. A number of studies [30–32] show that, for alloys and structural steels, the GTN model ensures better consistency of results obtained by numerical calculation (modelling) with experimental results than the HM model. By applying the GTN model to calculations, one is capable of analyzing the phenomenon of void growth, which allows locating the "weak" points in the structure, especially those susceptible to a local loss of load-carrying capacity.

From the present state of knowledge concerning the numerical modelling of steel plasticity, we can conclude that the modelling has been performed for small simple elements made of different types of steel or metallic alloys.

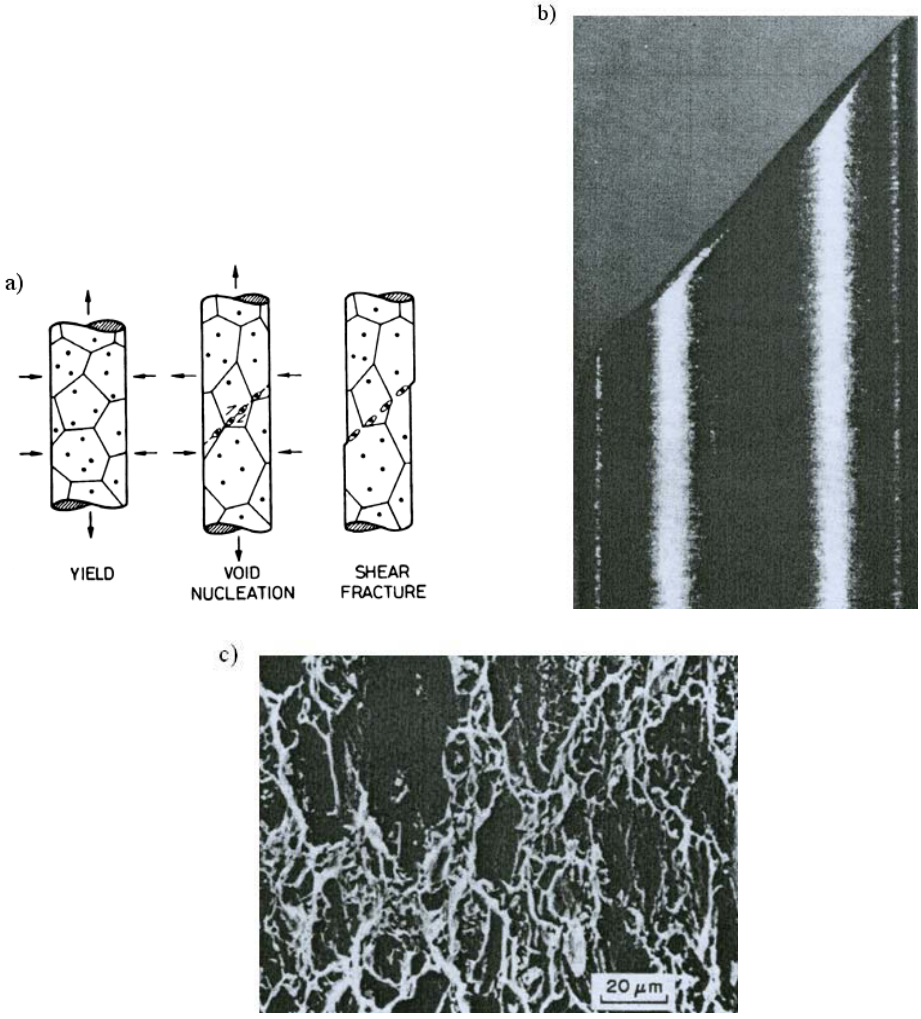

Fig. 1. a) Schematics of the nucleation, growth, and coalescence of voids leading to shear fracture, b) Macrophotograph of a 7075-T4 steel specimen subjected to tension which failed by shear fracture, c) Microphotograph of a 7075-T4 steel specimen which failed by shear fracture [22]

Most results are obtained by conducting simple strength tests, mainly tensile strength tests. Numerical analyses are performed using the method of best fit to material constants (the GTN model) for elements with predetermined geometries and strength properties. Microstructural parameters are frequently determined basing on the curve fit-

ting principle. There is no comprehensive approach that would allow performing numerical calculations for arbitrary elements. Another drawback is the lack of standardized microstructural parameters to develop a GTN model for steels used most commonly in engineering.

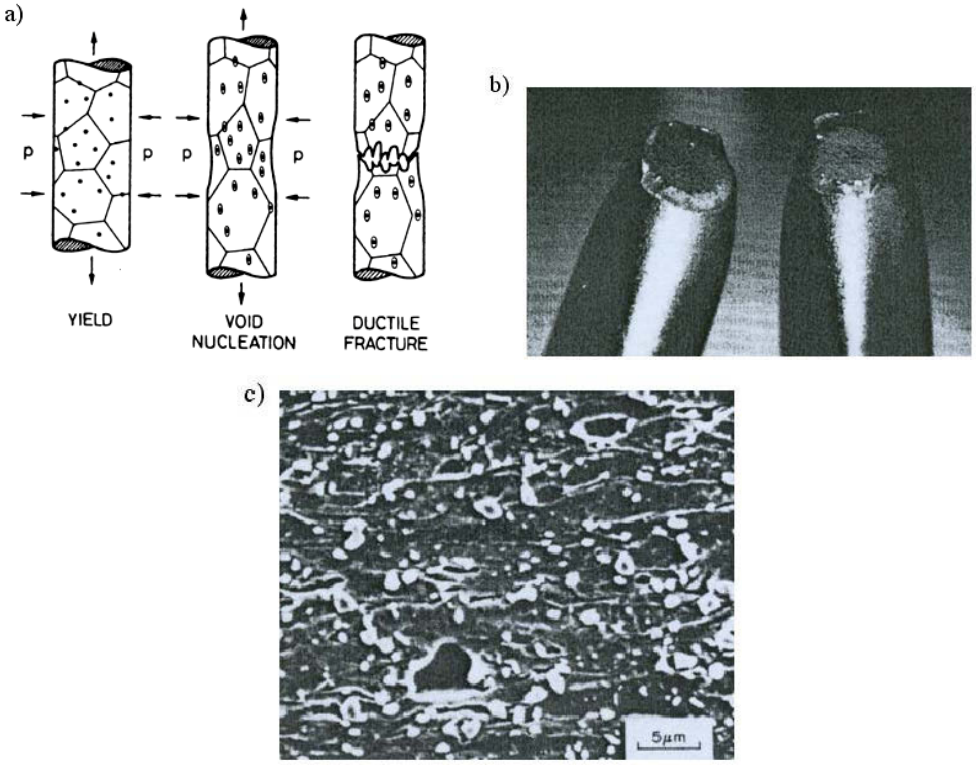

Figure 2. a) Schematics of the nucleation, growth and coalescence of voids leading to ductile fracture, b) Macrophotograph of a 1080 spheroidized steel specimen subjected to tension that failed by ductile fracture, c) A SEM microphotograph showing void growth in 1045 spheroidized steel subjected to axial tension, [22]

It is thus essential to develop a procedure for the numerical modelling of the load limit for any element subjected to any load, taking into account the effect of microfailure. This paper includes results of a load-carrying capacity analysis and discusses the void growth in S235JR steel elements in complex stress states basing on the Gurson–Tvergaard–Needelman (GTN) model, which takes into consideration the material structure.

The aim of the research was to determine the standardized material parameters for S235JR steel by conducting microstructural studies and standard tensile strength tests, followed by numerical modelling of data. As a result, it was possible to determine the parameters of the modified Gurson–Tvergaard–Needelman (GTN) model by analyzing the structure of S235JR steel.

The modified model was used to numerically analyse elements subjected to complex stress states, i.e. elements with different geometries as opposed to standard specimens subjected to tension.

The paper discusses the numerical calculation procedure, the result analysis, and the criteria of failure for S235JR steel obtained on the basis of the modified GTN model and the void growth. S235JR steel was selected for the tests because it is a common structural material in Poland. The data may be used for any analyses and expertise connected with the assessment of the load-carrying capacity and safety of structural elements and systems.

2. Gurson–Tvergaard–Needelman (GTN) damage model

As emphasized at the beginning, the classic Huber–Mises (HM) model cannot be used to analyse the effects of damage of microstructure on the load-carrying capacity and the strength of materials. Effective stresses (stress intensity) are a function of principal stresses according to the formula:

$$\bar{\sigma} = \frac{1}{\sqrt{2}} \sqrt{(\sigma_1 - \sigma_2)^2 + (\sigma_2 - \sigma_3)^2 + (\sigma_1 - \sigma_3)^2}, \tag{1}$$

where:

$\bar{\sigma}$ – von Mises effective stresses,

σ_1, σ_2, σ_3 – principal stresses.

The first model to take into consideration microdamage (pores, voids) was the Gurson model [5], which assumes that the proportion of voids in the plastic potential function is dependent on the void volume fraction f rather than the void volume, in accordance with the following relationship:

$$\Phi = \left(\frac{\bar{\sigma}}{\sigma_0} \right)^2 + 2f \cosh\left(\frac{3\sigma_m}{2\sigma_0} \right) - 1 - f^2 = 0, \tag{2}$$

where:

Φ – non-dilatational strain energy,

$\bar{\sigma}$ – von Misses effective stress according to the HM hypothesis,

σ_0 – strength of the material resulting from the tensile strength curve (yield stress),

σ_m – hydrostatic pressure (mean stress),

f – void volume fraction.

This condition was modified by Tvergaard [19] as:

$$\Phi = \left(\frac{\bar{\sigma}}{\sigma_0} \right)^2 + 2q_1 f^* \cosh\left(-q_2 \frac{3\sigma_m}{2\sigma_0} \right) - \left(1 + q_3 f^{*2}\right) = 0, \tag{3}$$

where:

f^* – actual void volume fraction,

q_i –Tvergaard coefficients describing the plastic properties of the material.

As can be seen from the GTN model, the influence of the plastic properties was taken into consideration by introducing the Tvergaard coefficients q_i, their values being as follows:

$$q_i = \begin{cases} q_1 = 1.5 \\ q_2 = 1.0 \\ q_3 = q_1^2 = 2.25 \end{cases} . \tag{4}$$

The above values have been confirmed in numerous studies as typical of many metals and steel grades. It should be noted that in the original Gurson condition, the coefficients characterizing the plastic properties of the material were $q_1 = q_2 = q_3 = 1$ [5]. When $f = 0$, the GTN yield condition (1) is reduced to form defined according to the HM condition. In the GTN model, the void volume fraction f^* is determined as follows:

$$f^* = \begin{cases} f & \text{for} \quad f \le f_c \\ f_c + \dfrac{\bar{f}_F - f_c}{f_F - f_c}\left(f - f_c\right) & \text{for} \quad f_c < f < f_F \\ \bar{f}_F & \text{for} \quad f \ge f_F \end{cases}, \tag{5}$$

where:

f_c – critical void volume fraction,

f_F – void volume fraction corresponding to the loss of material strength.

$$\bar{f}_F = \frac{q_1 + \sqrt{q_1^2 - q_3}}{q_3}.$$

An increase in the void volume fraction f is defined by the following relationship:

$$df = df_{gr} + df_{\text{nucl}} \tag{6}$$

where:

df_{gr} – time derivative of the volume fraction of voids existing in the material,

df_{nucl} – time derivative of the volume fraction of voids initiated by the deformation.

An increase in the volume fraction of voids df_{gr} existing in the material is defined as:

$$df_{gr} = \left(1 - f\right) d\varepsilon^{pl} : I \tag{7}$$

An increase in the volume fraction of voids initiated by the deformation df_{nucl} is defined as:

$$df_{nucl} = A\, d\bar{\varepsilon}_m^{pl} \tag{8}$$

An important parameter is the intensity of the nucleation (initiation) of voids A, defined as:

$$A = \frac{f_N}{s_N\sqrt{2\pi}} \exp\left[-\frac{1}{2}\left(\frac{\bar{\varepsilon}_m^{pl} - \varepsilon_N}{s_N}\right)\right], \tag{9}$$

where:

f_N – volume fraction of voids nucleated (initiated) on inclusions,
ε_N – mean strain of the void nucleation (initiation),
s_N – standard deviation of the nucleation strain,
$\bar{\varepsilon}_m^{pl}$ – mean plastic strain.

3. Determining the microstructural parameters of the GTN model

3.1. Microstructural analysis

The first step of the material analysis was to obtain microstructural images of S235JR steel [40] with a ferritic-perlitic matrix (Figure 3). As can be seen, there are a large number of non-metallic inclusions, which are mainly sulfides and brittle oxides. S235JR steel is reported to have appropriate metallurgical purity.

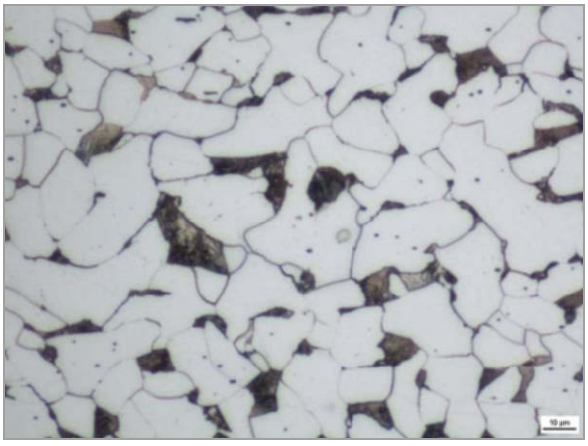

Fig. 3. SEM image of S235JR steel (transverse cross-section, middle layer) [40]

Sulfide inclusions were elongated in shape, with their length reaching 61.9 μm. Their distribution in the volume was irregular. They were arranged in bands. Table 1 shows the maximum diameter d_{max} and the extension ratio d_{max}/d_2, where d_2 is the equivalent diameter.

Other non-metallic inclusions found in the tested materials are uniaxial brittle oxide inclusions, which may co-occur with sulfide inclusions. To fully characterize non-metallic inclusions in the material, it was necessary to determine the basic stereological parameters:

- f_0 – void volume fraction,
- A – cross-sectional area,
- d_2 – equivalent diameter,
- d_{max} – maximum diameter,
- d_{max}/d_2 – extension ratio.

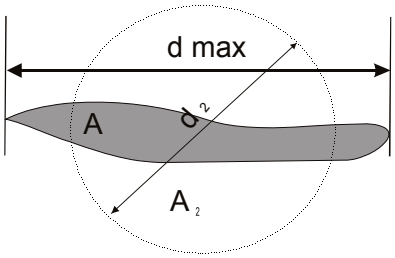

Fig. 4. Defining the stereological parameters for non-metallic inclusions [40]

Table 1. Comparing the results of the quantitative analysis of the images [40]

Cross-section	Cross-sectional area	Void volume fraction	n	A [μm^2]		d_2 [μm]		d_{min} [μm]		d_{max} [μm]		d_{max}/d_2	d_{max} (for the largest inclusion)
				mean value	std. dev	mean value	std. dev	mean value	std. dev	mean value	std. dev		
Transverse	central	0.17%	62	5.3	13.1	2.1	1.6	1.2	0.6	4.2	5.8	2.0	61.9
Transverse	outer	0.07%	66	2.5	3.3	1.5	0.9	1.0	0.5	2.5	2.2	1.6	18.2
Longitudinal	central	0.06%	68	1.8	5.5	1.3	0.8	1.1	0.6	1.6	1.6	1.3	22.0
Longitudinal	outer	0.03%	49	1.5	2.9	1.2	0.7	1.0	0.5	1.5	1.3	1.3	18.3

3.2 Tensile strength tests

The next step was to perform static tensile strength tests for specimens with a circular cross-section, with the diameter of the specimen ϕ = 10 mm, the length of the measuring base l_0 = 50 mm, and the primary cross-sectional area S_0 = 78.5 mm^2, according to [41]. Two ranges of traverse speed, i.e. 1 and 4 mm/min, were analysed. No impact of the speed was reported.

The average values obtained during the tests were as follows: the yield point (yield stress), $R_{0.2}$ = 318 MPa, the tensile strength, $R_{m.}$ = 446 MPa, and the displacement percentage, A_5 = 33.9%. Using the averaged $\sigma(\varepsilon)$ curve, it was possible to determine the nominal normal stress σ and the longitudinal strain ε.

Determining the microstructural parameters required modelling the data from the tensile strength tests (GTN model) numerically. The averaged tensile strength curve was approximated using the following equation:

$$\frac{\sigma}{\sigma_0} = \left(\frac{\sigma}{\sigma_0} + \frac{3G}{\sigma_0} \bar{\varepsilon}_m^{pl} \right)^N \tag{10}$$

where:

σ – stress,

σ_0 – yield stress,

G – coefficient of transverse elasticity,

$\bar{\varepsilon}_m^{pl}$ – mean plastic strain,

N – strain-hardening exponent.

Table 2. Strength parameters of S235JR steel according to Equation (10)

σ_0 [MPa]	σ_m [MPa]	G [MPa]	N
318	446	80 000	0.183

The data obtained during tensile strength tests were numerically modeled basing on the equation of the approximate curve (10). The Gurson–Tvergaard–Needelman (GTN) damage model takes into account the nucleation and growth of inclusion-related voids. The initial void volume fraction f_0 was 0.0017 = 0.17 %.

The critical void volume fraction, f_c, above which the material strength decreases, was 0.06. This value coincides with the results obtained by other authors [31]. As suggested by Richelsen and Tvergaard [42], the critical value of the void volume fraction, f_c, is dependent on the initial void volume fraction f_0. It ranges from f_c = 0.04 at f_0 = 0.0 to f_c = 0.12 at f_0 = 0.06. The calculated value, f_c = 0.06, is consistent with the experimental results.

The value of the void volume fraction corresponding to the loss of strength f_F was 0.667.

The Tvergaard parameters were: q_1 = 1.5, q_2 = 1.0, and q_3 = 2.25. The volume fraction of the nucleated voids f_N was 0.04, the average nucleation (initiation) strain of inclusion-related voids ε_N was 0.3, and the standard deviation of the strain s_N was 0.05.

Table 3. Microstructural parameters of the modified GTN model of S235JR steel

f_0	f_c	f_F	q_1	q_2	q_3	f_N	ε_N	f_N
0.0017	0.06	0.667	1.5	1.0	2.25	0.04	0.3	0.05

The numerical calculations were performed using the program based on the Finite Element Method, Abaqus Explicit version 6.7. The elements were modelled as axially symmetrical components using standard 4-node CAX4R elements [43].

Figure 5 shows a tensile strength curve determined numerically in the form of the load F versus displacement l function for the GTN model parameters.

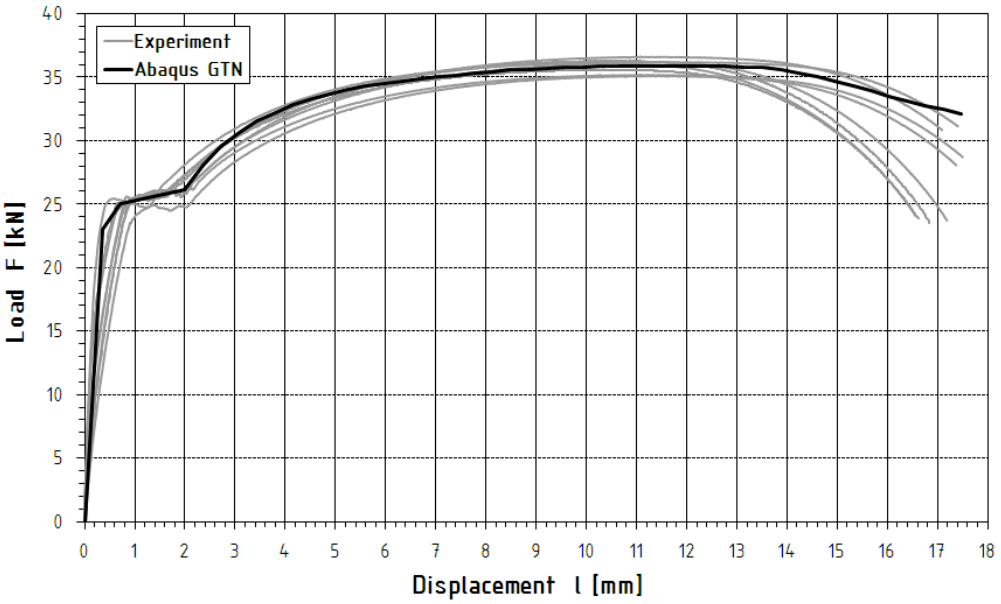

Fig. 5. Load-displacement $F(l)$ curves obtained through experiments and numerical analysis

4. Experimental and numerical modelling of load-carrying capacity and failure susceptibility in complex stress states

The analysis of load-carrying capacity and failure susceptibility was conducted using stretched ring-notched specimens with circular cross-sections for different notch radii ρ_0 (Figure 6).

The stress inside the specimens was calculated using the Bridgman analytical solution [44]. The triaxiality stress ratio $\sigma_m / \overline{\sigma}$ was determined as:

$$\frac{\sigma_m}{\overline{\sigma}} = \frac{1}{3} + \ln\left(\frac{r_0}{2\rho_0} + 1\right), \tag{11}$$

where:

$\sigma_m = (\sigma_{11}+\sigma_{22}+\sigma_{33})/3$ – mean stress,
$\overline{\sigma}$ – von Misses effective stress,
$2r_0$ – original minimum diameter,
ρ_0 – notch radius.

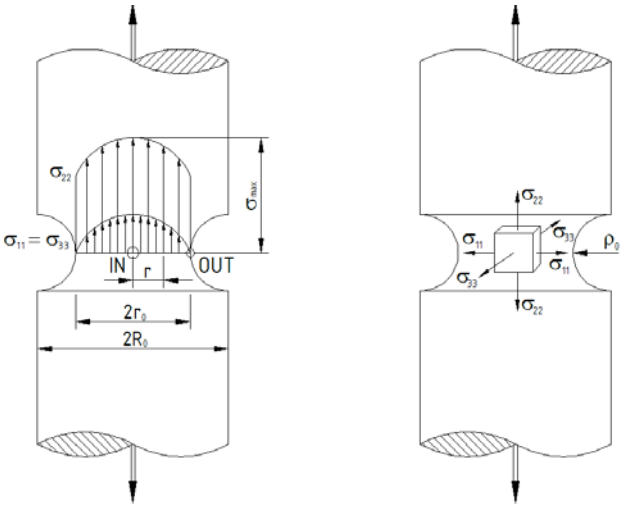

Fig. 6. Geometry and stress state components of a ring notched specimen

From relationship (11) it is clear that a change in the notch radius, ρ_0, has a significant effect on the stress state in the notch area. The analysis was conducted for elements with diameters $2R_0$ = 14.0 mm and $2r_0$ = 7.0 mm and notch radii ρ_0 ranging from 1.0 mm to 7.0 mm. It was possible to study the state of stress at different stress triaxiality ratios, ranging from $\sigma_m/\overline{\sigma}$ = 0.556 for ρ_0 = 7.0mm to $\sigma_m/\overline{\sigma}$ = 1.345 for ρ_0 = 1.0 mm (Table 4).

Table 4. Stress triaxiality ratio $\sigma_m/\overline{\sigma}$ for different notch radii

Notch radius	Stress triaxiality ratio
ρ_0 = 1.0mm	$\sigma_m/\overline{\sigma}$ = 1.345
ρ_0 = 1.5mm	$\sigma_m/\overline{\sigma}$ = 1.107
ρ_0 = 3.5mm	$\sigma_m/\overline{\sigma}$ = 0.739
ρ_0 = 7.0mm	$\sigma_m/\overline{\sigma}$ = 0.556

The load-carrying capacity analysis included tensile strength tests, during which specimens were subjected to static tension. The quantities measured were load F and displacement of points distributed symmetrically along the notch l, with the extensometer initial length being l_{0s} = 32.56 mm (Figure 7).

Two ranges of traverse speed were used: 1 and 4 mm/min. The speed was reported to have no effect on the results. The load vs. displacement curves are shown in Figures 10–13.

Fig. 7. View of a ring-notched round specimen subjected to tension in a complex stress state

The nature of the fracture (Figure 8) corresponds to the typical ductile failure, whose mechanism was described in the introduction and illustrated in Figure 2. The cracking resulted from the coalescence of voids through localized plastic strain. Macroscopically, the cracks were perpendicular to the maximum normal stress (tensile axis). In the central fracture area, there were numerous folds, which are attributable to the coalescence of voids due to slides down the planes inclined to the tensile axis at an angle of 30–45°. The cracks resulted from the slide and the coalescence of voids, with the slide occurring in the outer parts of the specimens. The cracks went along slide bands in the plane inclined to the tensile axis at an angle of 45°. For specimens with a high stress triaxiality ratio, at $\sigma_m / \overline{\sigma} > 1$ (where $\rho_0 = 1.0$ mm and $\rho_0 = 1.5$ mm, Figures 8a and b), the characteristic phenomenon was plasticity in a very small area surrounding the notch. For the other specimens (where $\rho_0 = 3.5$ mm and $\rho_0 = 7.0$ mm, Figs 8c and d), the plasticity was more visible; it extended from the bottom of the notch in the longitudinal direction, like in tensile strength tests conducted for smooth specimens.

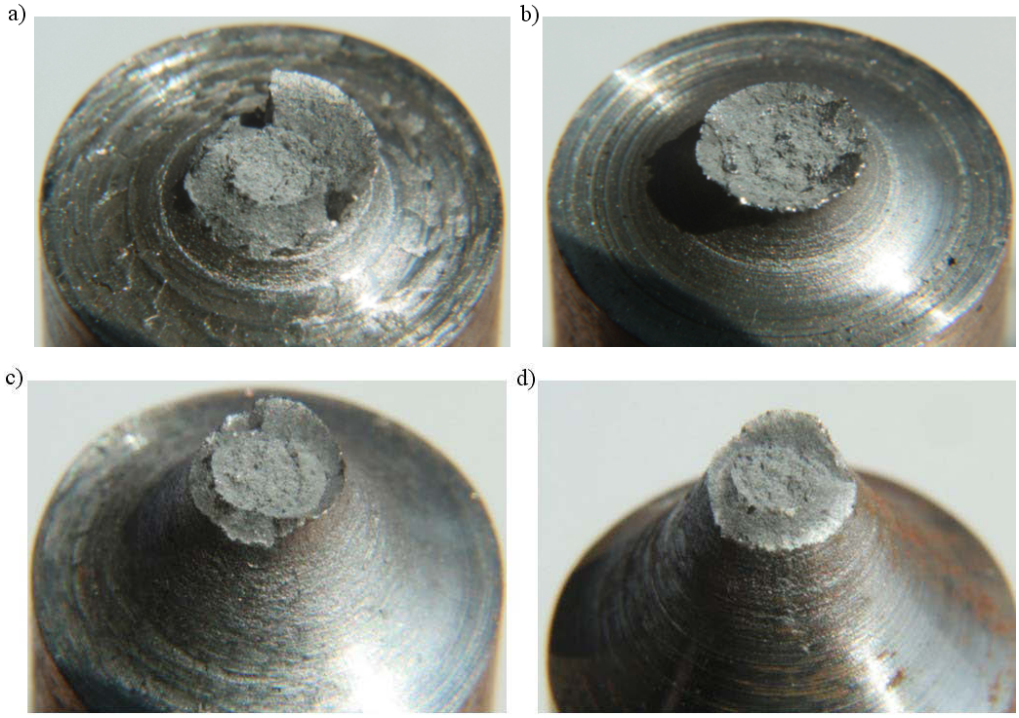

Fig. 8. Macrographs of fracture surfaces of specimens under tension in a complex stress state: a) ρ_0 = 1.0 mm, b) ρ_0 = 1.5 mm, c) ρ_0 = 3.5 mm, d) ρ_0 = 7.0 mm

The next stage of the analysis was numerical calculations. It was necessary to develop a procedure for modelling specimens by using the GTN model, verify the experimental results, and analyse the growth of microvoids and their effect on the load-carrying capacity.

The numerical calculations were performed using a program based on the Finite Element Method (Abaqus Explicit version 6.7). The elements modelled were the same as those used during the tensile strength tests. The ring-notched specimens with a circular cross-section were subjected to static tension in the complex stress state, the notch radius ρ_0 ranging from 1.0 mm to 7.0 mm. The modelling was performed for axially symmetrical standard 4-node CAX4R elements [42]. Because of the symmetry, the modeling was conducted only for half-specimens (Figure 9). The height of the numerical models corresponded to half of the extensometer length, i.e. 16.28 mm.

The Gurson-Tvergaard-Needleman (GTN) damage model required using the nonlinear explicit dynamic analysis. To compare the results, it was essential to perform numerical calculations based on the classic Huber-Misses model using a static analysis. The load-carrying capacity was defined by plotting the load F against displacement l (Figures 10–13).

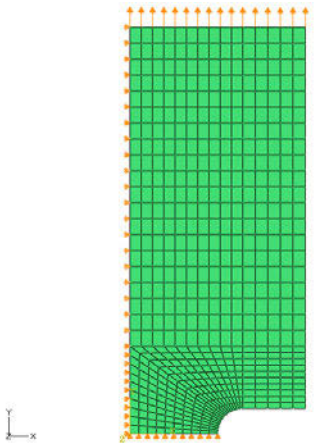

Fig. 9. Numerical model of a ring-notched element with a circular cross-section

The void growth was analysed basing on the changes in the void volume fraction that occurred during the plasticity process and the effect of voids on the stress state described by the stress triaxiality ratio $\sigma_m / \bar{\sigma}$. The relationship between the void volume fraction and the stress triaxiality ratio $\sigma_m / \bar{\sigma}$ in the function of displacement l was determined for a point inside a specimen designated as IN and for the bottom of the notch at a point designated as OUT (according to Figure 6).

As can be seen from the $F(l)$ curves plotted for the ring-notched specimens subjected to tension, the load F, which was determined by applying the GTN model and the non-linear explicit dynamic analysis, was lower than that obtained with the classic Huber-Misses model and the static analysis. It was found that the material porosity significantly affected the tensile strength and the load-carrying capacity.

It should be noted that the tensile strength curves obtained by applying the GTN model and the non-linear explicit dynamic analysis are consistent with the experimental results, and thus are closer to the real ones. This is not true about the results obtained by applying the HM model and the static analysis.

The GTN model assumes that for elements with the notch radius ρ_0 ranging from 1.0 mm to 3.5 mm, which corresponds to a maximum load, the numerical data are consistent with the experimental results. For a specimen with the notch radius equal to 7.0 mm, the values of load determined numerically were lower than those obtained experimentally (Figure 13). In a wider range, the numerically calculated values of the load F were lower than the real ones (Figures 10–13).

The $F(l)$ curves plotted for elements with $\rho_0 = 1.0$ mm and $\rho_0 = 1.5$ mm show that the maximum values of the load F (load-carrying capacity) were achieved at $l = 0.5$ mm (Figures 10 and 11). For the other elements with $\rho_0 = 3.5$ mm and $\rho_0 = 7.0$ mm, the load-carrying capacity was accomplished at $l = 0.68$ mm and $l = 0.85$ mm, respectively (Figures 12 and 13).

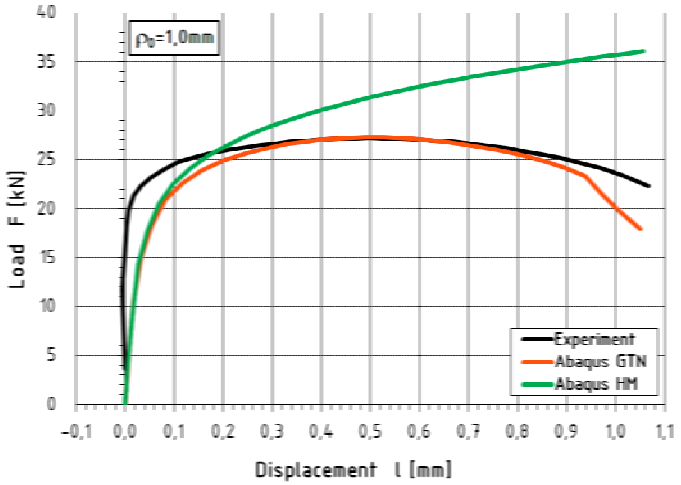

Fig. 10. Load-displacement $F(l)$ curves for a specimen with the notch radius ρ_0 = 1.0 mm

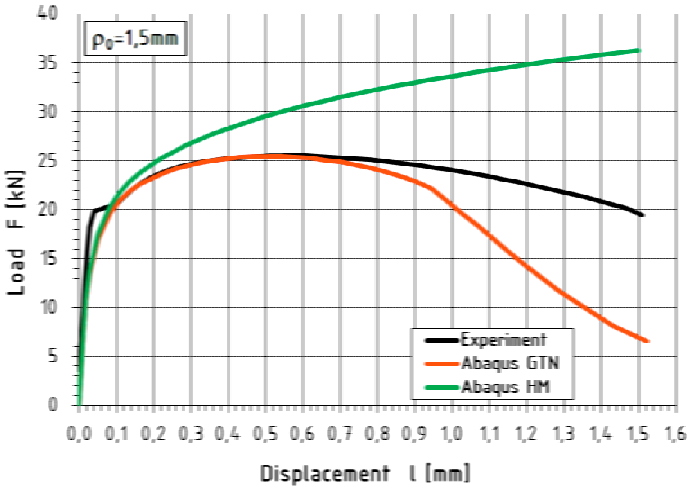

Fig. 11. Load-displacement $F(l)$ curves for a specimen with the notch radius ρ_0 = 1.5 mm

For each specimen, there was a fall in the load capacity followed by the element failure after the maximum strength was reached. This applies both to the experimental results and the numerical simulation data obtained by means of the GTN model. For elements with ρ_0 = 1.0 mm and ρ_0 = 1.5 mm and the resulting high stress triaxiality ratio, one can determine the point beyond which there occurs a sharp decrease in load corresponding to the displacement l equal to 0.94 mm. In the range from the maximum load-carrying capacity to the failure, the differences in load were bigger during the experiments than during the numerical calculations.

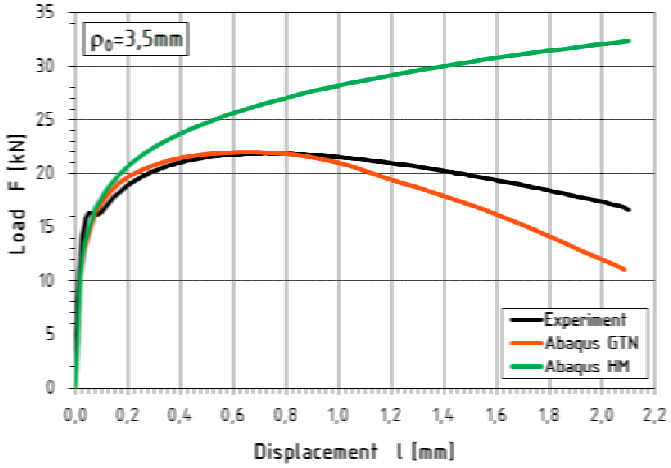

Fig. 12. Load-displacement $F(l)$ curves for a specimen with the notch radius $\rho_0 = 3.5$ mm

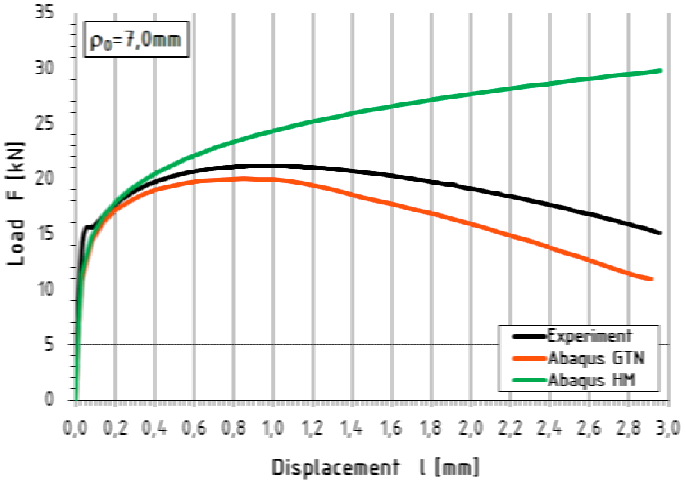

Fig. 13. Load-displacement $F(l)$ curves for a specimen with the notch radius $\rho_0 = 7.0$ mm

An increase in the void volume fraction was observed for the displacements corresponding to the maximum load-carrying capacity, i.e. $l = 0.5$ mm for specimens with $\rho_0 = 1.0$ mm and $\rho_0 = 1.5$ mm and $l = 0.68$ mm and $l = 0.85$ mm for specimens with $\rho_0 = 3.5$ mm and $\rho_0 = 7.0$ mm, respectively. Figures 14 and 18 illustrate the increase in the void volume fraction for specimens with the notch radius $\rho_0 = 1.0$ mm ($\sigma_m / \overline{\sigma} > 1$) and $\rho_0 = 3.5$ mm ($\sigma_m / \overline{\sigma} < 1$). The initial increase in the void volume fraction was particularly intensive in the outer part of the specimen (point OUT in Figure 14).

Beyond the maximum load-carrying capacity, there was a more rapid increase in the void growth rate, especially for elements with a higher stress triaxiality ratio, $\sigma_m / \overline{\sigma} > 1$ (Figure 14). When $\sigma_m / \overline{\sigma} > 1$, the more rapid increase in the void growth rate resulted from the considerable decrease in the load-carrying capacity; for elements with ρ_0 = 1.0 mm and ρ_0 = 1.5 mm, the displacement was l = 0.94 mm. Beyond that point, the growth of voids inside the specimen (point IN) was more rapid than outside (point OUT). During the process of further plasticity, the voids inside an element grew in number more intensively and rapidly (Figure 14). Figures 15a and b show maps of the void volume fraction for elements with the highest stress triaxiality ratio, i.e. $\sigma_m / \overline{\sigma}$ = 1.345 at ρ_0 = 1.0 mm. The map of the void volume fraction in Figure 15a corresponds to l = 0.94 mm, and accordingly, to a sudden drop in the load-carrying capacity. Figure 15b presents a map of the void volume fraction after that point was reached. In the first case, the highest void volume fraction was in the outer part (point OUT), while in the other case, the increase in voids was more visible in the inner part (point IN). It could thus be concluded that the rupture would go from the inside to the outside.

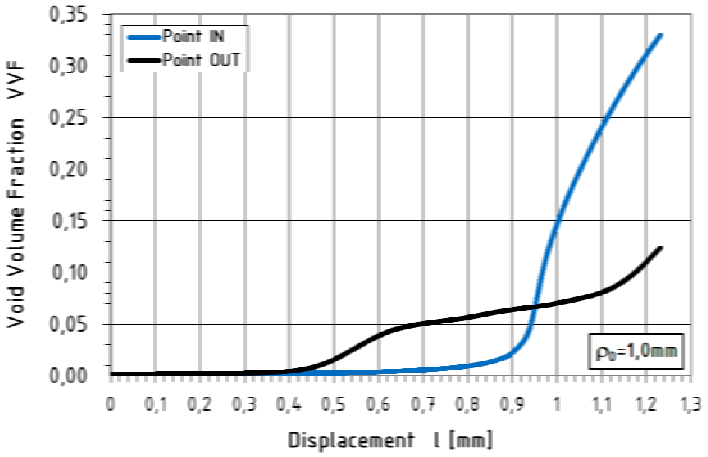

Fig. 14. Void volume fraction versus displacement curve for a specimen with ρ_0 = 1.0 mm

Another characteristic phenomenon observed during the numerical simulation was that the damage growth occurred in a very small volume of material, directly in the plane of the smallest cross-section near the notch bottom (Figures 15 and 19).

The phenomena described above are particularly strong for elements with a high stress triaxiality ratio, i.e. $\sigma_m / \overline{\sigma} > 1$. When $\sigma_m / \overline{\sigma} < 1$, that is for elements with ρ_0 = 3.5 mm and ρ_0 = 7.0 mm, the phenomena were less intensive. The void volume growth rate was lower for $\sigma_m / \overline{\sigma} < 1$ than for $\sigma_m / \overline{\sigma} > 1$. The phenomenon was reflected in the experimental results and the numerical simulations data. The specimens

with ρ_0 = 1.0 mm and ρ_0 = 1.5 mm were reported to fail much sooner. It is thus clear that the material failure caused, for instance, by an increase in the number of voids, will occur sooner if the stress traixiality ratio is high, $\sigma_m / \overline{\sigma} > 1$.

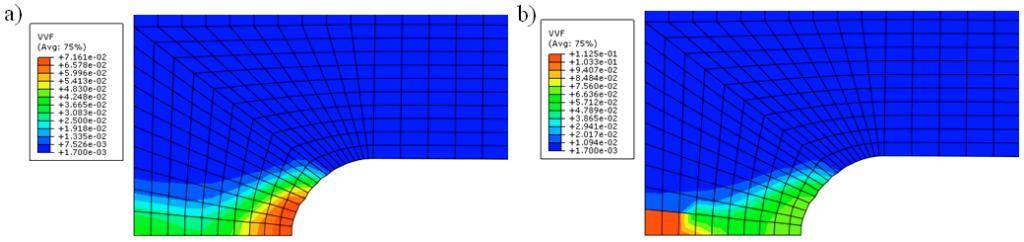

Fig. 15. Void volume fraction maps for a specimen with ρ_0 = 1.0 mm, a) l = 0.94 mm, b) l = 0.97 mm

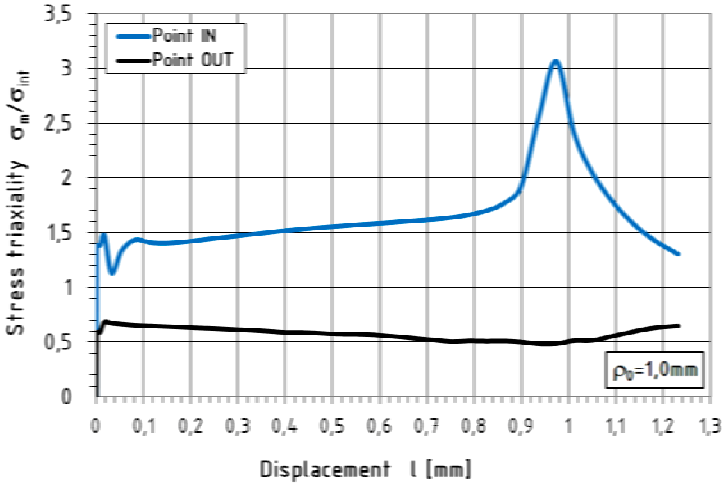

Fig. 16. Triaxiality stress ratio versus displacement curves for a specimen with ρ_0 = 1.0 mm

As can be seen, the increase in the void volume fraction affected the load-carrying capacity and strength of the specimens considerably. This influence was particularly visible when $\sigma_m / \overline{\sigma} > 1$. It can be concluded that for elements with $\sigma_m / \overline{\sigma} > 1$, the microstructural failure (void growth) was closely related to the changes in the stress state.

The void volume fraction at the moment of failure ranged between 20 and 45%. The value of 45% was obtained for elements with ρ_0 = 1.5 mm at test duration of 13s. For the other specimens, the value was in the range of 20–29%. The minimum void volume fraction was approximately 20%. It was possible to determine the criterion of failure basing on the GTN model. It should be noted that the result refers to one rate of

deformation. If the load conditions are different, the result may be different, too. It seems that the influence of the deformation rate on the rate and intensity of void growth needs to be analysed separately.

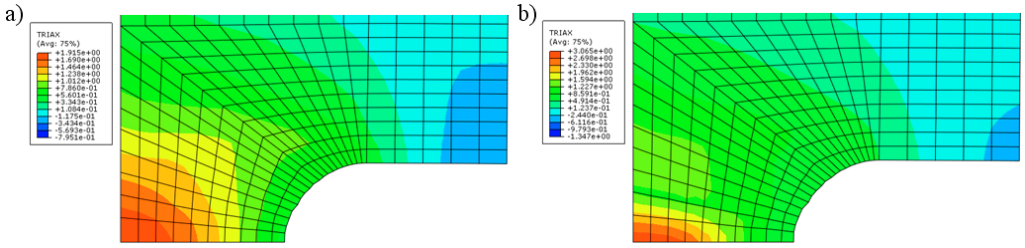

Fig. 17. Triaxiality stress ratio maps for a specimen with ρ_0 = 1.0 mm: a) l = 0.90 mm; b) l = 0.97 mm

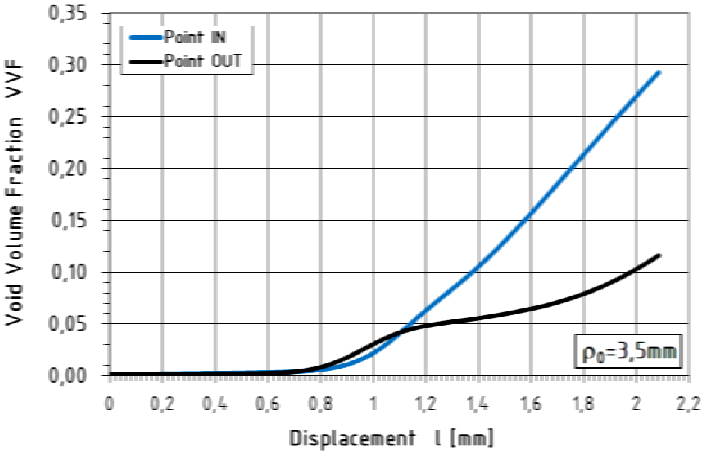

Fig. 18. Void volume fraction versus displacement curves for a specimen with ρ_0 = 3.5 mm

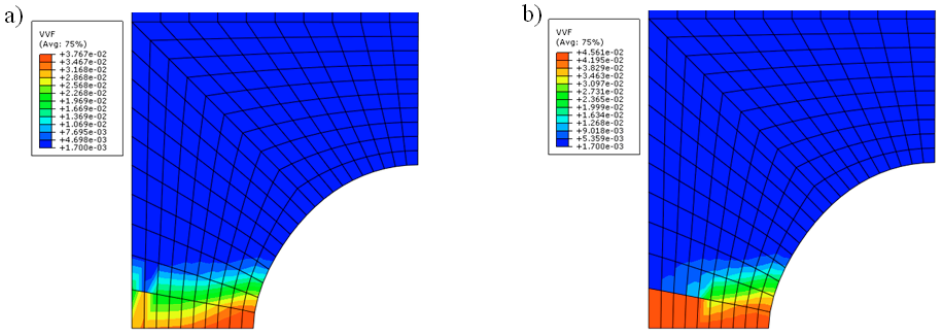

Fig. 19. Void volume fraction maps for a specimen with ρ_0 = 3.5 mm, a) l = 1.05 mm, b) l = 1.12 mm

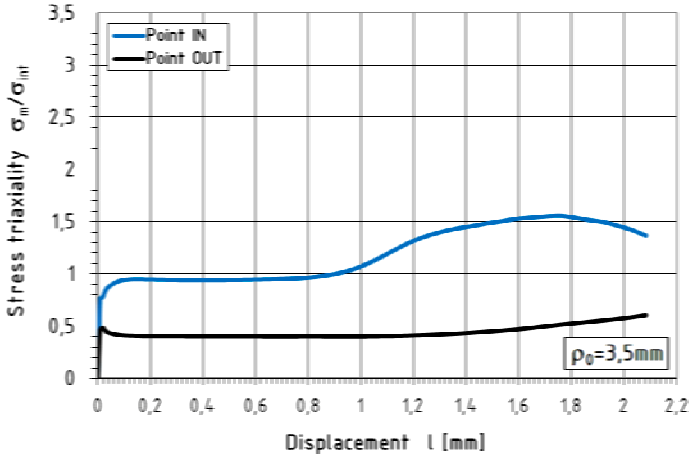

Fig. 20. Triaxiality stress ratio versus displacement curves for a specimen with $\rho_0 = 3.5$ mm

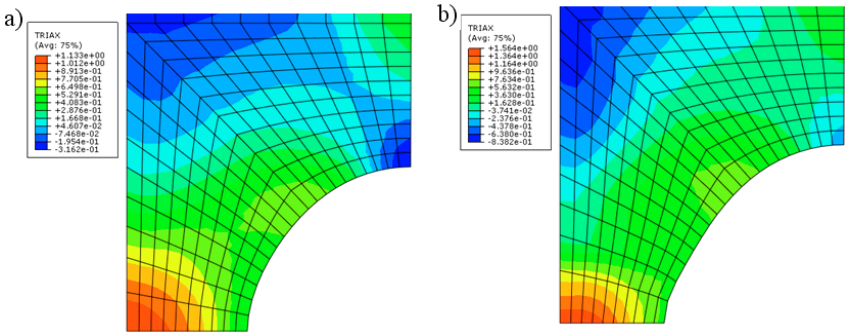

Fig. 21. Triaxiality stress ratio maps for a specimen with $\rho_0 = 3.5$ mm, a) $l = 1.05$ mm, b) $l = 1.76$ mm

Another objective of the study was to evaluate the impact of the stress state on the load-carrying capacity of elements and the material microdamage. The stress state was expressed as the stress triaxiality ratio, while the microdamage was defined by the increase in the void volume fraction. Prior to the rapid decline in the load-carrying capacity, there was a slight increase in the stress triaxiality ratio $\sigma_m / \overline{\sigma}$ in the inner part of the elements and a slight decrease of this ratio in the outer. This corresponds to l = 0–0.85 mm for elements with $\rho_0 = 1.0$ mm and $\rho_0 = 1.5$ mm. When l reached 0.85 mm, there was a significant increase in $\sigma_m / \overline{\sigma}$ in the inner part; it rose until $\sigma_m / \overline{\sigma} = 3.1$ at $l = 0.96$ mm for an element with $\rho_0 = 1.0$ mm. It is clear that the rapid decline in the load-carrying capacity and the rate of increase in the void volume fraction were related to the rapid change in the stress state reflected by a sudden increase in the stress triaxiality ratio in the inner part. In the analysed range, there was a slight

increase in $\sigma_m / \overline{\sigma}$ in the outer part of the elements. After the rapid decrease in the load capacity at $l > 0.96$ mm, there was a decrease in the stress triaxiality ratio in the inner part until $\sigma_m / \overline{\sigma} \approx 1.4$, which corresponded to the initial value of $\sigma_m / \overline{\sigma}$. Figures 17a and b show maps of the stress triaxiality ratio $\sigma_m / \overline{\sigma}$ for an element with $\rho_0 = 1.0$ mm at $l = 0.90$ mm and $l = 0.97$ mm.

Changes in the stress triaxiality ratio $\sigma_m / \overline{\sigma}$ coinciding with microstructural changes were observed also in elements with $\rho_0 = 3.5$ mm and $\rho_0 = 7.0$ mm; their intensity, however, was considerably smaller (Figures 20 and 21).

5. Final remarks and conclusions

The paper deals with the results of the load capacity analysis and the growth of microstructure damage taking the form of voids for elements made of S235JR steel subjected to complex stress states. The modified Gurson–Tvergaard–Needelman (GTN) model taking account of the material structure was used.

The objective of the study was to determine the standardized material parameters for S235JR steel by conducting a microstructural analysis and standard tensile strength tests with their numerical modelling. The parameters were obtained by means of the modified GTN model taking into account the steel structure.

The modified model was used for the numerical analysis of elements under the action of complex stress states, whose geometries were different from those of the standardized specimens. The numerical calculations including the analysis of maximum values and the criteria of failure for S235JR steel based on the modified GTN model and the development of microvoids.

Because of the extensive use of S235JR steel in the building industry in Poland, the results can be applied to various analyses and expertise with the aim of estimating the load-carrying capacity and the structural safety of elements.

The following are the conclusions drawn from the analysis results:

– By applying the modified GTN model, which takes into account the real microstructural parameters for S235JR steel elements, one is capable of estimating the failure loads resulting from plastic fracture.

– The tensile strength curves obtained by using the modified GTN model taking into consideration the real microstructural parameters and the non-linear explicit-type dynamic analysis were consistent with the experimental results, i.e. the real results, in contrast with the data obtained by means of the HM model and the static analysis.

– The parameters of the modified GTN model taking account of the real microstructural parameters of S235JR steel determined on the basis of the microstructural analysis, tensile strength tests and numerical analysis, were used to good effect during the analysis of elements subjected to complex stress states.

– Initially, the void growth was very intensive in the outer part of the specimens. After the maximum load-carrying capacity was reached, the rate of the void growth

was higher, especially for elements with a higher stress triaxiality ratio, i.e. $\sigma_m / \overline{\sigma} > 1$. When $\sigma_m / \overline{\sigma} > 1$, the increase in the void growth rate corresponded to the rapid fall in the element load capacity. Once the point was reached, the voids grew in number more rapidly in the central part of the elements rather than in the outer part. It can be assumed that the failure occurring in the central part is crucial to the load capacity of the whole element.

– An increase in the void volume fraction is observed in a very small volume of the material; it occurs in the plane of the smallest cross-section near the notch bottom.

– An increase in the void volume fraction affected the load-carrying capacity and strength of analysed elements. Effect was more visible for the elements with $\sigma_m / \overline{\sigma} > 1$. When $\sigma_m / \overline{\sigma} > 1$, the void growth was attributable to changes in the stress state.

– The specimens with the notch radius ρ_0 equal to 1.0 mm or 1.5 mm was reported to fail earlier than the other specimens. It can be assumed that failure caused, for instance, by an increase in the void growth, will occur more rapidly in elements with a high stress triaxiality ratio (i.e. $\sigma_m / \overline{\sigma} > 1$).

– The minimum void volume fraction of 20% corresponding to the element failure was determined by applying the modified GTN model, which took into consideration the real microstructural parameters. The value can be treated as a criterion of failure for the S235JR specimens subjected to complex stress states.

– By analyzing the damage which takes the form of voids, one is able to analyse the load-carrying capacity, and accordingly, the safety of structural elements. As failure is expected to occur once the void volume fraction reaches a critical value, it is possible to apply this procedure to analyse the failure states of structural elements made of S235JR steel basing on the modified GTN model taking account of the real microstructural parameters of this material.

– The modified GTN model, which takes account of the real microstructural parameters of S235JR steel, was used to analyse the growth of voids, and their number and location in an element. Basing on the results, it was possible to establish the weak points of the structure, i.e. areas particularly susceptible to loss of load-carrying capacity. The material structure was reported to be responsible for the load-carrying capacity of the whole element.

Acknowledgements

The research reported herein was conducted as part of Project R04 007 01 funded over the period 2006–2010 from education budget.

References

[1] Kachanov L.: *Time of the rupture process under creep conditions*, Izv. Akad Nauk SSSR, Otd. Tekh. Nauk, No. 8, 1958, pp. 26–31.

[2] Lemaitre J.: *How to use damage mechanics*, Nuclear Eng. and Design, Vol. 80, No. 2, 1984, pp. 233–245.
[3] Lemaitre J.: *A continuum damage mechanics model for ductile fracture*, J. Eng. Mat. and Technology, Vol. 107, No. 1, 1985, pp. 83–89.
[4] Murakami S., Proc. 2nd Int. Conference on Constitutive Laws for Engineering Materials, ed. Desai, C.S. and Krempl E., Elsevier, 1987.
[5] Gurson A.L.: *Continuum theory of ductile rupture by void nucleation and growth: Part I – yield criteria and flow rules for porous ductile materials*, J. Eng. Mat. and Tech., Vol. 99, No. 1, 1977, pp. 2–15.
[6] Suquet P.: *Plasticité et homomogénéisation*, Thése Doctorat d'Etat, Univ. Paris VI, 1982.
[7] Cordebois J.P., Sidoroff F.: *Endommanegament anisotrope en elasticité et plasticité*, J. Méc. Théor. Appl., Numero Spécial, 1982, pp. 45–60.
[8] Tvergaard V.: *Material failure by void coalescence in localized shear bands*, DCAMM Report No. 221, Techn. Univ. of Denmark, Lyngby, 1981, pp. 1–26.
[9] Tvergaard V.: *Numerical study of localization in a void sheet*, DCAMM Report No. 337, Techn. Univ. of Denmark, Lyngby, 1988, pp. 1–19.
[10] Rousselier G.: *Finite deformation constitutive relations including ductile fracture damage*, IUTAM Symp. on Three-dimensional constitutive relations and ductile fracture, Eds. Dourdan, Nemat-Nasser, North-Holland, 1981, pp. 331–355.
[11] Rousselier G.: *Les modéles de rupture ductile et leurs possibilités actuelles dans le cadre de l'approche locale de la rupture*, Moret-sur-Loing, 1986, France.
[12] Dragon A., Chihab A.: *Quantifying of ductile fracture damage evolution by homogenization approach*, SMiRT 8, Brussels, 1985.
[13] Chow C.L., Lu T.J.: *An analytical and experimental study of mixed-mode ductile fracture under nonproportional loading*, Int. J. Damage Mech., Vol. 1, No. 2, 1992, pp. 191–236.
[14] Voyiadjis G.Z., Kattan P.I.: *A plasticity-damage theory for large deformation of solids, Part I: theoretical formulation*, Int. J. Eng. Sci., Vol. 30, No. 9, 1992, pp. 1089–1108.
[15] Murzewski J.: *Brittle and ductile damage of stochastically homogeneous solids*, Int. J. Damage Mech., Vol. 1, No. 3, 1992, pp. 276–289.
[16] Mou Y.H., Han R.P.S.: *Damage evolution in ductile materials*, Int. J. Damage Mech, Vol. 5, No. 3, 1996, pp. 241–258.
[17] Saanouni K., Foster C., Ben Hatira F: *On the anelastic flow with damage*, Int. J. Damage Mech., Vol. 3, No. 2, 1994, pp. 140–169.
[18] Taher S.F., Baluch M.H., Al-Gadhib A.H.: *Towards a canonical elastoplastic damage model*, Eng. Fracture Mech., Vol. 48, No. 2, 1994, pp. 151–166.
[19] Tvergaard V.: *Influence of voids on shear band instabilities under plane strain condition*, Int. J. Fracture Mech., Vol. 17, No. 4, 1981, pp. 389–407.
[20] Tvergaard V., Needleman A.: *Analysis of the cup cone fracture in a round tensile bar*, Acta Metall., Vol. 32, No. 1, 1984, pp. 157–169.
[21] Needleman A., Tvergaard V.: *Analysis of the ductile rupture in notched bars*, J. Mech. and Physics Solids, Vol. 32, No. 6, 1984, pp. 461–490.
[22] Terlinck D., Zok F., Embury J.D., Ashby M.F.: *Fracture mechanism maps in stress space*, Acta Metall., Vol. 36, No. 5, 1998, pp. 1213–1228.
[23] Aoki S., Amaya K., Sahashi M., Nakamura T.: *Identification of Gurson's material constants by using Kalman filter*, Comp. Mech., Vol. 19, No. 6, 1997, pp. 501–506.

[24] Corigliano A., Mariani S., Orsatti B.: *Identification of Gurson-Tvergaard material model parameters via Kalman filtering technique. I. Theory*, Int. J. Fracture, Vol. 104, No. 4, 2000, pp. 349–373.
[25] Nowak Z., Stachurski A.: *Identification of an augmented Gurson model parameters for plastic porous media*, Foundation of Civil and Environmental Engineering, No. 2, 2002, pp. 141–150.
[26] Nowak Z.: *Metoda identyfikacji w mechanice materiałów ciągliwych*, IPPT PAN, Warszawa, 2006.
[27] Springmann M., Kuna M.: *Identification of material parameters of the Gurson-Tvergaard-Needleman model by combined experimental and numerical techniques*, Comp. Mat. Sc., Vol. 32, No. 3–4, 2005, pp. 544–552.
[28] Chhibber R., Arora N., Gupta S.R., Dutta B.K.: *Estimation of Gurson material parameters in bimetallic weldments for the nuclear reactor heat transport piping system*, Jour. Mech. Eng. Sc., Vol. 222, No. 12, 2008, pp. 2331–2349.
[29] Hayhurst D., Trąmpczyński W., Leckie F.: *On the role of cavity nucleation in creep deformation and fracture*, Acta Metall., Vol. 31, No. 10, 1983, pp. 1537–1542.
[30] Biel-Gołaska M., Gołaski L.: *Modelowanie procesu pękania odlewów kolikowych i cienkościennych ze stopu Al-Si poddanych obciążeniom dynamicznym*, Projekt badawczy Nr PB 1037/T08/95/09, Instytut Odlewnictwa, Kraków, 1998.
[31] Lachowski J., Biel-Gołaska M.: *Symulacja odkształcania plastycznego i ewolucji uszkodzeń w przestrzennych stanach obciążenia*, VII Krajowa konferencje Mechaniki Pękania, Kielce-Cedzyna, 23–25 IX 1999, Zeszyty Naukowe Politechniki Świętokrzyskiej, Kielce, 1999, pp. 261–268.
[32] Biel-Gołaska M., Gołaski L., Lachowski J., Żuczek R.: *Analiza rozwoju uszkodzeń w stopach odlewniczych*, Raport KBN, Nr 8008/00, Instytut Odlewnictwa, Kraków, 2000.
[33] Hang Z.L., Thaulow C., Ødegård J.: *A complete Gurson model approach for ductile fracture*, Eng. Fract. Mech., Vol. 67, No. 2, 2000, pp. 155–168.
[34] Reusch F., Svendsen B., Klingbeil: *Local and non-local Gurson-based ductile damage and failure modelling a large deformation*, European J. of Mech. A/Solids, Vol. 22, No. 6, 2003, pp. 779–792.
[35] Hashemi S.H., Howard I.C., Yates J.R., Andrews R.M.: *Micro-mechanical damage modelling of notched bar testing of modern line pipe steel*, The 15th European Conference of Fracture – *Advanced fracture mechanics for life and safety*, Stockholm, August 11–13, 2004, p. 8.
[36] Münlich U., Brocks W.: *Regularization behaviour of nonlocal Gurson-type model*, The 15th European Conference of Fracture – *Advanced fracture mechanics for life and safety*, Stockholm, August 11–13, 2004, p. 8.
[37] Samal M.K., Seidenfuss M., Roos E., Dutta B.K., Kushwaha H.S.: *A mesh-independent Gurson–Tvergaard–Needleman damage model and its application in simulating ductile fracture behaviour*, J. Mech. Eng. Sc., Vol. 223, No. 2, 2008, pp. 283–292.
[38] Cricrì G.: *Consistent use of the Gurson-Tvergaard damage model for the R-curve calculation*, Convegno Nazionale IGF XX, Torino, 2009, pp. 138–150.
[39] J. Pastor, Ph. Thoré.: *Gurson model for porous pressure sensitive materials*, D. Weichert, A. Ponter (eds.), Limit States of Materials and Structures, Springer Science+Business Media B.V., 2009.

[40] *Określenie struktury materiałów (pobranych z konstrukcji) analiza porównawcza z parametrami stali wzorcowej*, Raport z badań w ramach projektu *Opracowanie oraz wstępna weryfikacja procedury diagnozowania metodą emisji akustycznej konstrukcji metalowych ze szczególnym uwzględnieniem mostów stalowych*, Politechnika Warszawska, Wydział Inżynierii Materiałowej, Warszawa, 2008.
[41] PN-EN 1002-1, *Metale. Próba rozciągania*. Część 1: *Metoda badania w temperaturze otoczenia*.
[42] Richelsen A.B, Tvergaard V.: *Dilatant plasticity or upper bound estimates for porous ductile solids*, Acta Metall. Mater., Vol. 42, No. 8, 1994, pp. 2561–3577.
[43] *ABAQUS Analysis user's manual, Version 6.7*, ABAQUS, Inc. and Dassault Systèmes, 2007.
[44] Bridgman P.W.: *Studies in large flow and fracture*, McGraw-Hill, New York, 1952.

Analiza nośności elementów pracujących w złożonych stanach naprężenia z uwzględnieniem wpływu uszkodzeń miktrostrukturalnych

W artykule przedstawiono wyniki analizy nośności elementów wykonanych ze stali S235JR pracujących w złożonych stanach naprężenia z uwzględnieniem wpływu uszkodzeń mikrostrukturalnych. Opracowano zmodyfikowany model Gursona–Tvergaarda–Needelmana (GTN) dla stali S235JR poprzez wykonanie badań mikrostrukturalnych, przeprowadzenie normowych prób rozciągania oraz ich modelowane numeryczne. Zmodyfikowany model GTN zastosowano w analizie numerycznej elementów pracujących w złożonych stanach naprężeń. Stwierdzono zgodność uzyskanych wyników w stosunku do rezultatów badań wytrzymałościowych. Opisano sposób prowadzenia obliczeń numerycznych wraz z analizą możliwych do uzyskania wyników oraz określono kryteria zniszczenia stali S235JR w oparciu o zmodyfikowany model GTN i rozwój mikrouszkodzeń.